A generalized exact volume constraint method for the topology optimization based on the nonlinear reaction-diffusion equation

Yi CUI[1)], Sungmin YOON[3)], Shaojie GUI[2)], Toru TAKAHASHI[4)], Toshiro MATSUMOTO[5)]

1) Nagoya University (〒 464-8603 Furo-cho, Chikusa-ku, Nagoya, E-mail: yi.cui@mae.nagoya-u.ac.jp)
2) Nagoya University (〒 464-8603 Furo-cho, Chikusa-ku, Nagoya, E-mail: yoon.sungmin.v8@f.mail.nagoya-u.ac.jp)
3) Nagoya University (〒 464-8603 Furo-cho, Chikusa-ku, Nagoya, E-mail: gu.shaojie.e7@f.mail.nagoya-u.ac.jp)
4) Nagoya University (〒 464-8603 Furo-cho, Chikusa-ku, Nagoya, E-mail: toru.takahashi@mae.nagoya-u.ac.jp)
5) Nagoya University (〒 464-8603 Furo-cho, Chikusa-ku, Nagoya, E-mail: t.matsumoto@nuem.nagoya-u.ac.jp)

From a intuitive perspective, exact boundary representation emerges as the most favorable approach for topology optimization of structural systems based on the finite element method (FEM). Under exact boundary representation, the material domain can be precisely defined, granting the flexibility to impose arbitrary boundary conditions on newly generated boundaries throughout the optimization process. This newfound capability is achieved through the recently introduced exact volume constraint method, which effectively addresses the convergence challenges associated with exact boundary representation. However, one key consideration that has not yet been explored is the potential nonlinearity of the reaction-diffusion equation governing the evolution of the level set function. Consequently, the primary objective of this study is to expand upon the proposed topology optimization methodology, which incorporates exact boundary representation, to account for nonlinear aspects of the reaction-diffusion equation. Subsequently, we will conduct a comparative analysis of the results obtained using various proportional constants denoted as K in relation to the level set function ϕ.

Key Words: Exact boundary representation, Volume constraint, Topology optimization, Topological derivative, Finite element method

1. Introduction

In the realm of modern manufacturing processes, structural topology optimization has assumed a pivotal role, courtesy of the relentless advancement in computer technology. The SIMP (Solid Isotropic Material with Penalization) method, a well-entrenched approach in topology optimization [1, 2], employs density distribution to interpolate material constants. In its numerical implementation, a nonzero lower bound for Young's modulus is prescribed to avert singularities when solving the stress equilibrium equation. To mitigate the limitations stemming from the pronounced grayscale issues inherent to the original SIMP method, Yamada et al. introduced the level-set method, particularly one based on solving the Reaction Diffusion Equation (RDE) [3]. This approach has subsequently gained traction as an appealing alternative for addressing a spectrum of topology optimization challenges [4, 5, 6, 7, 8, 10]. Notably, topology optimizations involving updated body-fitted meshes [6, 7, 8] have demonstrated success by adopting variations of the augmented Lagrangian method for volume-constrained problems. Nonetheless, in the aforementioned studies, it remains essential to employ mesh structures within the void domain, coupled with the imposition of a nonzero lower bound, to circumvent singularity issues in solving the stress equilibrium equation. As we have demonstrated and compared in the appendix of our recent work [10], this approach can indeed achieve convergence, even when utilizing the conventional (inexact) volume constraint method. This stability is attributed to the presence of a nonzero lower bound within the void domain, akin to the SIMP method, which serves to stabilize the optimization process. In stark contrast to the prevailing body-fitted remeshing paradigm, the attainment of exact boundary representation (where no mesh is assigned within the void domain) has remained an elusive goal. Additionally, it is worth noting that the widely adopted topological derivative [12] for sensitivity analysis should ideally be

Received Oct. 9, 2023, Accepted Nov. 5. 2023

coupled with exact boundary representation, given its premise of hole insertion rather than density distribution. The challenge of achieving exact boundary representation likely stems from the adoption of the conventional (inexact) volume constraint method [13, 14, 15]. In contrast, the recently proposed exact method for volume constraint [10] has enabled such convergence under the exact boundary representation. However, in the prior work [10], the feasibility of achieving exact boundary representation while considering a nonlinear RDE has yet to be investigated. On the other hand, there have already been a handful of well-established works on RDE-based topology optimization [11, 3] by applying conventional volume constraint methods. Therefore, the primary objective of this study is to extend the proposed topology optimization methodology with exact boundary representation to accommodate the nonlinear RDE, and subsequently, compare the outcomes obtained with different proportional constants K as a function of the level set function ϕ.

2. Methodology

To perform the structural topology optimization, first we define the level-set function ϕ. The following level set function ϕ is introduced to represent the material domain Ω, the material boundary $\partial\Omega$ and the complementary void domain $D\backslash\Omega$:

$$\begin{cases} 0 < \phi(\boldsymbol{x}) \leq 1 & \text{for } \boldsymbol{x} \in \Omega, \\ \phi(\boldsymbol{x}) = 0 & \text{for } \boldsymbol{x} \in \partial\Omega, \\ -1 \leq \phi(\boldsymbol{x}) < 0 & \text{for } \boldsymbol{x} \in D\backslash\Omega. \end{cases} \tag{1}$$

A characteristic function as defined below is necessary in performing the volume integration.

$$\chi_\phi = H(\phi) = \begin{cases} 0 & \text{if } \phi < 0, \\ 1 & \text{if } \phi \geq 0. \end{cases} \tag{2}$$

The minimum compliance problem by considering the level set function $\phi(\boldsymbol{x}) \in [-1, 1]$ as a spatial function inside the design domain can be formulated as follows:

$$\inf_{\phi} \; F(\phi) = l(\boldsymbol{u}), \tag{3}$$

$$\text{subject to } \; a(\boldsymbol{u}, \boldsymbol{v}) = l(\boldsymbol{v}), \tag{4}$$

$$\text{and } G(\phi) = \int_D \chi_\phi \, \mathrm{d}\Omega - V_{\text{req}} \leq 0. \tag{5}$$

The weak form of the governing equation reads

$$a(\boldsymbol{u}, \boldsymbol{v}) := \int_\Omega \boldsymbol{\varepsilon}(\boldsymbol{u}) : \mathbb{C} : \boldsymbol{\varepsilon}(\boldsymbol{v}) \, \mathrm{d}\Omega, \tag{6}$$

$$l(\boldsymbol{v}) := \int_{\Gamma_N} \boldsymbol{t} \cdot \boldsymbol{v} \, \mathrm{d}\Gamma. \tag{7}$$

Here D is the design domain, V_{req} is the volume constraint, $\boldsymbol{u}$ is the displacement, $\boldsymbol{v}$ is the virtual displacement, $\boldsymbol{\varepsilon}(\boldsymbol{u})$ is the corresponding total strain, $\mathbb{C}$ is the fourth-order elasticity tensor and the vector $\boldsymbol{t}$ is the given external boundary load. Since the boundary representation becomes exact, the same weak form is based on the reconstructed material domain Ω:

$$\int_\Omega \boldsymbol{\varepsilon}(\boldsymbol{u}) : \mathbb{C} : \boldsymbol{\varepsilon}(\boldsymbol{v}) \, \mathrm{d}\Omega = \int_{\Gamma_N} \boldsymbol{t} \cdot \boldsymbol{v} \, \mathrm{d}\Gamma. \tag{8}$$

Once K depends on ϕ, the nonlinear boundary value problem to update the level set function is as follow.

$$\begin{cases} \frac{\partial \phi}{\partial t} = K(\phi)(-\overline{\mathcal{T}} + \Lambda + \tau\nabla^2\phi) & \text{in } D, \\ \frac{\partial \phi}{\partial n} = 0 & \text{on } \partial D\backslash\partial\Gamma_N, \\ \phi = 1 & \text{on } \partial\Gamma_N. \end{cases} \tag{9}$$

Here t is the fictitious time, $K(\phi)$ is the coefficient of proportionality, τ is a regularization parameter for the fictitious interface energy, and $\mathcal{T}$ stands for the topological derivative and can be expressed as:

$$\mathcal{T} = -\boldsymbol{\sigma} : \mathbb{P} : \boldsymbol{\varepsilon}. \tag{10}$$

The normalized topological derivative can be expressed as:

$$\begin{cases} \overline{\mathcal{T}} = C_0 \mathcal{T}, \\ C_0 = \frac{\int_D \mathrm{d}\Omega}{2\int_D |\mathcal{T}| \mathrm{d}\Omega}. \end{cases} \tag{11}$$

The polarization tensor $\mathbb{P}$ for the plane stress case can be found, for example, in Lopes et al.:[12]

$$\mathbb{P} = \frac{1}{1+\nu}\left(2\mathbb{I} - \frac{1-3\nu}{2(1-\nu)}\mathbf{I} \otimes \mathbf{I}\right). \tag{12}$$

Verification has been made by comparing the above topological derivative with the corresponding result from the direct FEM calculation. During the numerical implementation, it is the normalized topological derivative $\overline{\mathcal{T}}$ that has been used.

Our finite element analysis has been carried out by FreeFEM++,[16, 17] and it is an open-source software package that requires formulating the weak form of governing equation to carry out the finite element simulation. As for the remeshing process, the open-source software package Mmg has been employed. For illustration, the design domain D, the material domain Ω and the void domain $D\backslash\Omega$ are shown in Fig. 1, alongside the geometry and boundary conditions.

2.1. The augmented Lagrangian method for volume-constrained problems[13, 14, 15, 18]

For the nonlinear RDE, the Augmented Lagrangian for volume-constrained problems, as referred as the conventional (inexact) method, for the current step $t_{n+1} = t + \Delta t$, is formulated as:

$$\Lambda_{n+1} = \begin{cases} \frac{1}{V}(q_n + r_n G_n) & \text{if } G_n \geq -\frac{q_n}{r_n} \\ 0 & \text{if } G_n < \frac{q_n}{r_n} \end{cases} \tag{13}$$

The positive scalar q is the Lagrange multiplier for the inequality constraint, r is the penalty parameter, and η is a normalization factor introduced to stabilize the results of sensitivity analysis. It should be

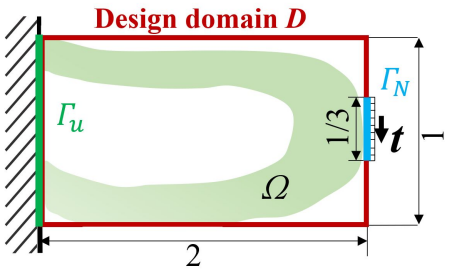

(a) 2D center-load case (plane stress)

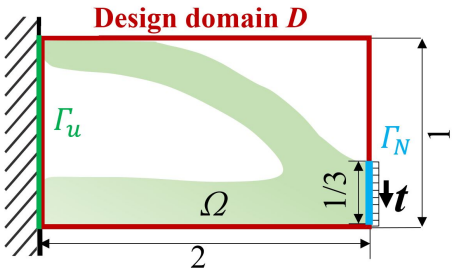

(b) 2D lower-load case (plane stress)

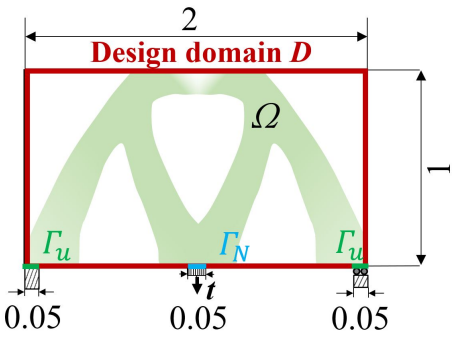

(c) 2D bridge-like case (plane stress)

Fig. 1: The schematic of 2D minimum compliance problems. The magnitude of the boundary traction is 10 kPa. The Young modulus is 70 GPa, and the Poisson ratio is 0.33. For the level set function, $\frac{\partial \phi}{\partial n} = 0$ on $\partial D \backslash \Gamma_N$ and $\phi = 1$ on Γ_N

noted that all above parameters are from the previous optimization step t_n:

$$G_n = \int_D \chi(\phi_n)\, \mathrm{d}\Omega - V_{\text{req}}. \tag{14}$$

Only after knowing the current Λ_{n+1} (and hence ϕ_{n+1}) can all other parameters be updated as follows to be used in the next optimization step. Given the initial values of the two parameters and the constant γ are $q_1 = 0$, $r_1 = 0.1$ or 0.2 and $\gamma = 1.025.$, they are updated in the optimization process by:

$$\begin{cases} q_{n+1} = & q_n + r_n \max(G_n, -q_n/r_n), \\ r_{n+1} = & \gamma r_n. \end{cases} \tag{15}$$

2.2. The exact volume constraint method[10]

In contrast to the inexact method, our proposed exact volume constraint method is virtually parameter-free. The pivotal idea of the exact volume constraint method is to split the original RDE into two terms by letting:

$$\phi = \phi^* + \Lambda\, \hat{\phi}. \tag{16}$$

Once split, ϕ^* within the interval from t to $t + \Delta t$ is governed by:

$$\begin{cases} \frac{\partial \phi^*}{\partial t} = K(\phi|_t)(-\overline{\mathcal{T}} + \tau \nabla^2 \phi^*) & \text{in } D, \\ \frac{\partial \phi^*}{\partial n} = 0 & \text{on } \partial D \backslash \partial \Gamma_N, \\ \phi^* = 1 & \text{on } \partial \Gamma_N, \\ \phi^*|_t = \phi|_t. \end{cases} \tag{17}$$

By subtracting Eq. (17) from the original RDE Eq. (9), after the elimination of Λ, $\hat{\phi}$ satisfies the following initial boundary value problem:[10]

$$\begin{cases} \frac{\partial \hat{\phi}}{\partial t} = K(\phi|_t)(1 + \tau \nabla^2 \hat{\phi}) & \text{in } D, \\ \frac{\partial \hat{\phi}}{\partial n} = 0 & \text{on } \partial D \backslash \partial \Gamma_N, \\ \hat{\phi} = 0 & \text{on } \partial \Gamma_N, \\ \hat{\phi}|_t = 0. \end{cases} \tag{18}$$

Given that $K(\phi|_t)$ remains unchanged from time t to $t + \Delta t$, the division of ϕ into two terms with their respective governing equations remains unaffected. The volume constraint can then be viewed as an implicit equation for Λ:

$$g(\Lambda) = \int_D \chi_{\phi(\Lambda)} \mathrm{d}\Omega - V_{\text{req}} = 0. \tag{19}$$

For Eq. (19), Newton-Raphson iteration is needed to find Λ[10]. In the beginning of the optimization loop, as required to calculate the volume integration, a smoothed Heaviside function capable of converging to the rigorous Heaviside function has been adopted. Instead of an invariantly smoothed Heaviside function, a stepwise one is adopted:

$$H(\phi) = \frac{1}{2}\tanh(k\phi) + \frac{1}{2}. \tag{20}$$

In the numerical implementation, we simply let $k = n^q + 1$ ($q = 0.5$) at the nth time step. Besides, all other conditions, such as the use of the smoothed Heaviside function have been made identical in the comparison between the two volume constraint methods. The flowchart to implement the topology optimization by updating ϕ without (Loop 1) and with (Loop 2) the reconstruction of the domain Ω is shown in Fig. 2. The level set function from using the coarse mesh in Loop 1 has been interpolated onto the fine mesh in Loop 2. The introduction of Loop 1 aims to reduce the remeshing cost. For both loops, a convergence criterion below is adopted for ϕ (0.01 for loop 1 and 0.02 for loop 2):

$$\|\phi|_{t+\Delta t} - \phi_t\|_{L^\infty} < \epsilon_\phi. \tag{21}$$

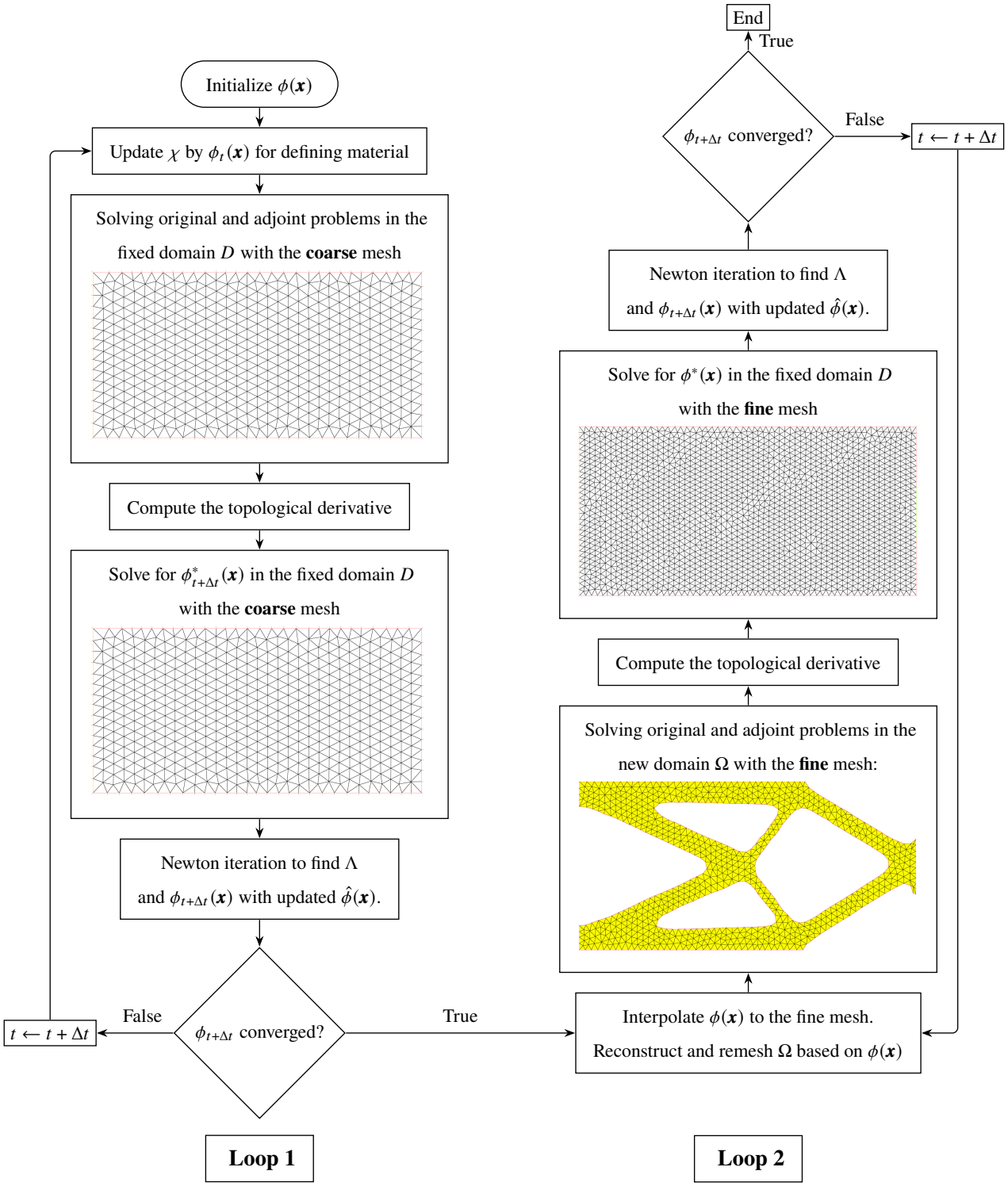

Fig.2: Flowchart of the two-loop approach. For stress analysis, Loop 1 (left) adopts a fixed mesh, while Loop 2 (right) reconstructs and remesh the material domain. The difference from [10] is that the RDE for $\hat{\phi}$ needs to be solved per each optimization step.

3. Results and discussions

In this section, we will examine and discuss the results of topology optimization, comparing the outcomes obtained through both the inexact and the exact volume constraint methods introduced in the preceding section. For all cases, the initial structure is a uniformly distributed characteristic function χ.

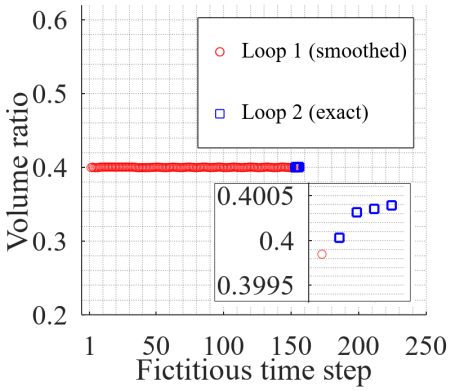

(a) $K(\phi) = 1$

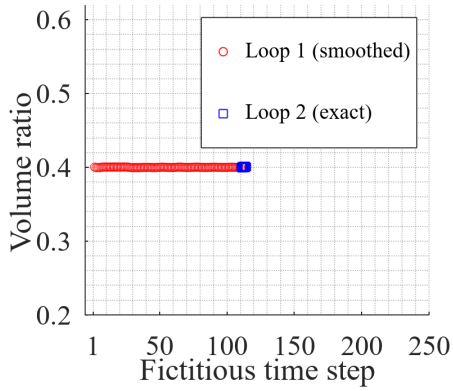

(b) $K(\phi) = 0.5 + \cos(0.5\pi\phi)$

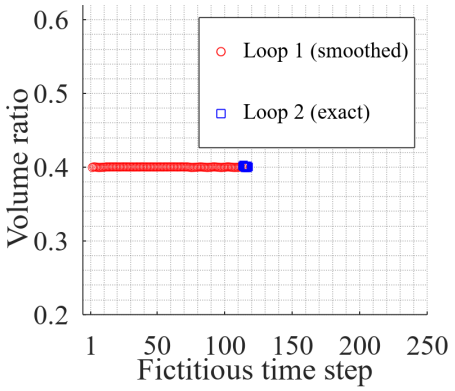

(c) $K(\phi) = 0.5 + \sin(0.5\pi\phi)$

Fig. 3: Volume ratio by using the exact volume constraint method for the center-load case considering three different $K(\phi)$

For the center-load case, as depicted in Fig. 3, the exact volume constraint method consistently maintains the material volume ratio within the design domain at precisely 0.4, meeting the specified relative error tolerance of 0.001 during Loop 1. It's important to note that the material volume ratio in Loop 1 includes a certain degree

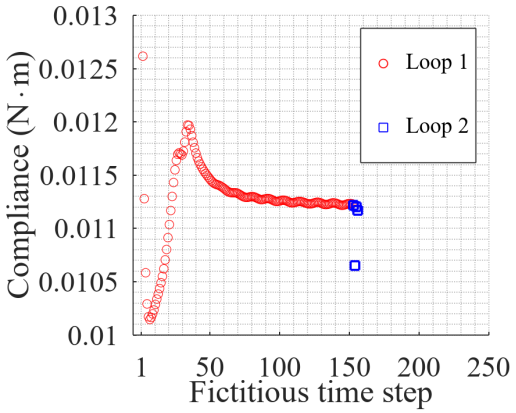

(a) $K(\phi) = 1$

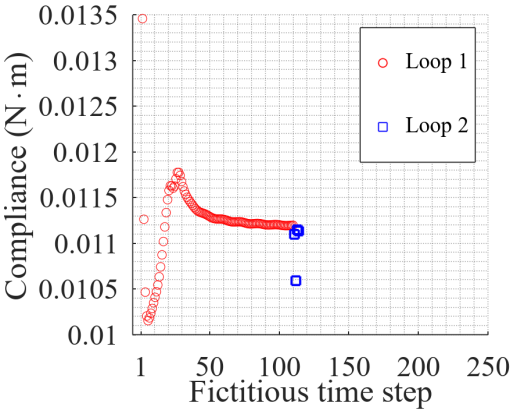

(b) $K(\phi) = 0.5 + \cos(0.5\pi\phi)$

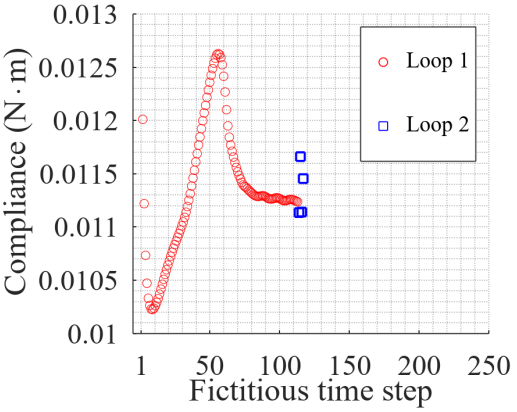

(c) $K(\phi) = 0.5 + \sin(0.5\pi\phi)$

Fig. 4: Structural compliance by using the exact volume constraint method for the center-load case considering three different $K(\phi)$

of grayscale, which neither represents material nor void. During Loop 2, the grayscale is eliminated through material domain reconstruction and remeshing, resulting in an exact material volume ratio. The remeshing process only marginally increases the actual relative error tolerance compared to Loop 1. This demonstrates the validity of our proposed exact volume constraint method for nonlinear RDE, even though the governing equation for $\hat{\phi}$ must be solved for each optimization step. Regarding the structural compliance in Fig. 4, the initially low value before step 50 is attributed to the significant grayscale presence. Among different $K(\phi)$ values, the convergence is slowest when $K = 1$, while the other two converge

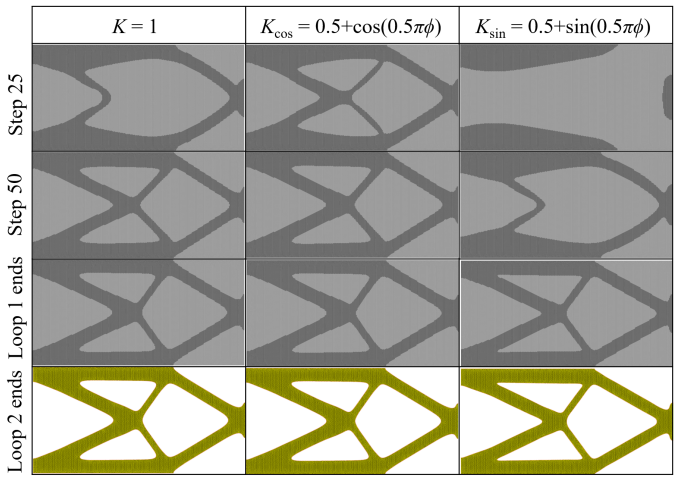

Fig. 5: Structural change during optimization by using the exact volume constraint method for the center-load case considering three different $K(\phi)$

at a similar rate. For the structural changes during optimization in Fig. 5, when $K = 1$ and $K(\phi) = 0.5 + \cos(0.5\pi\phi)$, the structure at step 50 closely resembles the final converged structure in Loop 1. However, the emergence of the structure is slowest when using $K(\phi) = 0.5 + \sin(0.5\pi\phi)$. Comparing the final optimized structures, the upper and lower triangular openings in the case of $K(\phi) = 0.5 + \sin(0.5\pi\phi)$ are noticeably wider than those in the other two cases.

The lower-load case, as depicted in Fig. 6, demonstrates that our proposed exact method for volume constraint is valid regardless of the boundary conditions. Regarding structural compliance in Fig. 7, the initially low value before step 50 can be attributed to the significant grayscale presence. Among the different $K(\phi)$ values, $K(\phi) = 0.5 + \cos(0.5\pi\phi)$ results in faster convergence, while $K(\phi) = 0.5 + \sin(0.5\pi\phi)$ results in the slowest convergence.

In the context of structural changes during optimization in Fig. 8, both $K = 1$ and $K(\phi) = 0.5 + \cos(0.5\pi\phi)$ lead to a structure at step 50 that closely resembles the final converged structure in Loop 1. Conversely, the emergence of the structure is slowest when using $K(\phi) = 0.5 + \sin(0.5\pi\phi)$. When comparing the final optimized structures, the upper triangular opening in the case of $K(\phi) = 0.5 + \sin(0.5\pi\phi)$ is notably wider than in the other two cases. Additionally, in Fig. 8, more holes are visible in the case of $K(\phi) = 0.5 + \sin(0.5\pi\phi)$.

The bridge-like case, as depicted in Fig. 9, once again demonstrates that our proposed exact method for volume constraint is valid regardless of the boundary condition. Regarding structural compliance in Fig. 10, the initially low value before step 50 can be attributed to the significant grayscale presence. Among different $K(\phi)$ values, $K(\phi) = 0.5 + \cos(0.5\pi\phi)$ results in fastet convergence, while $K(\phi) = 0.5 + \sin(0.5\pi\phi)$ results in the slowest convergence. When considering structural changes during optimization in Fig. 11, the slowest emergence of the structure occurs when using $K(\phi) = 0.5 + \sin(0.5\pi\phi)$, and its final optimization result slightly differs from the other two.

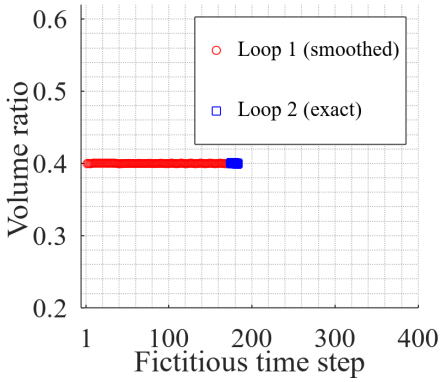

(a) $K(\phi) = 1$

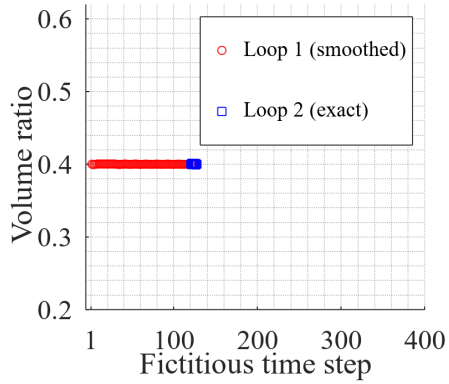

(b) $K(\phi) = 0.5 + \cos(0.5\pi\phi)$

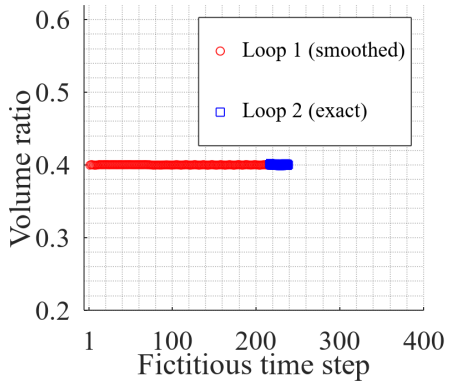

(c) $K(\phi) = 0.5 + \sin(0.5\pi\phi)$

Fig. 6: Volume ratio by using the exact volume constraint method for the lower-load case considering three different $K(\phi)$

The results obtained using the conventional volume constraint method, referred to as the 'inexact method,' will be examined hereafter. The center-load case, as observed in Fig. 12, highlights a problem with the inexact method for volume constraint during Loop 2, where achieving convergence during the reconstruction and remeshing of the material domain becomes challenging. In Loop 2, both $K(\phi) = 0.5 + \cos(0.5\pi\phi)$ and $K(\phi) = 0.5 + \sin(0.5\pi\phi)$ exhibit significant fluctuations in both Fig. 12 and Fig. 13.

When considering structural changes during optimization in Fig.

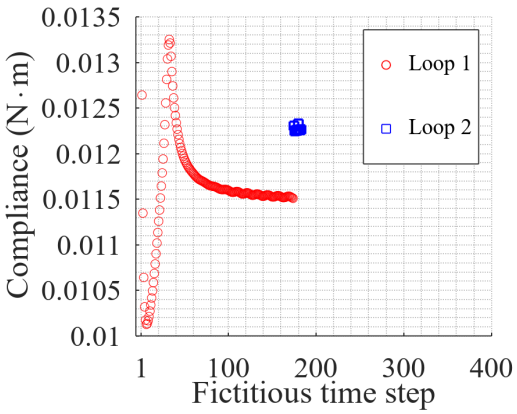

(a) $K(\phi) = 1$

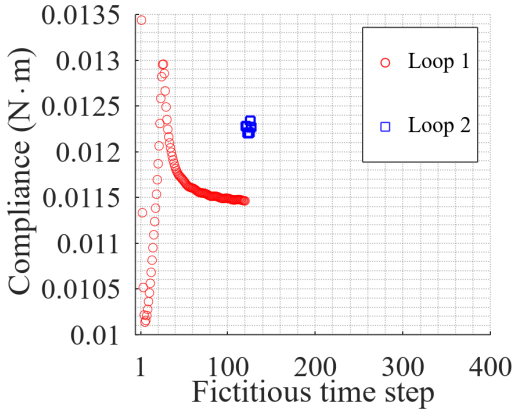

(b) $K(\phi) = 0.5 + \cos(0.5\pi\phi)$

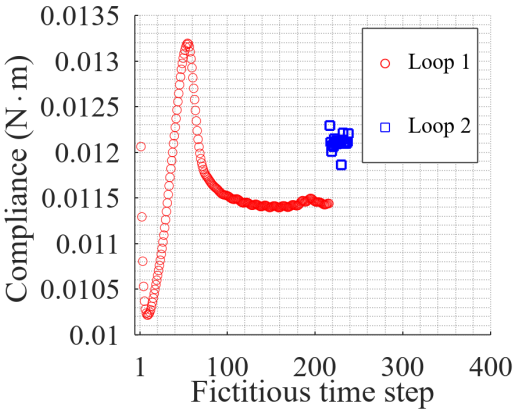

(c) $K(\phi) = 0.5 + \sin(0.5\pi\phi)$

Fig. 7: Structural compliance by using the exact volume constraint method for the lower-load case considering three different $K(\phi)$.

14, the slowest emergence of the structure occurs when using $K(\phi) = 0.5 + \sin(0.5\pi\phi)$, and regardless of the choice of $K(\phi) = 0.5 + \cos(0.5\pi\phi)$, convergence remains elusive during Loop 2. This difficulty in achieving convergence during Loop 2 is inherent to the inexact method for volume constraint, as it operates as an explicit forward time-stepping method and faces challenges when dealing with void domains without mesh.

The lower-load case, as observed in Fig. 15, highlights a problem with the inexact method for volume constraint during Loop 2, where achieving convergence during the reconstruction and remeshing of the material domain becomes challenging. In Loop 2, both $K(\phi) = 0.5 + \cos(0.5\pi\phi)$ and $K(\phi) = 0.5 + \sin(0.5\pi\phi)$ exhibit significant fluctuations in both Fig. 15 and Fig. 13. When considering structural changes during optimization in Fig. 17, the slowest emergence of the structure occurs when using $K(\phi) = 0.5 + \sin(0.5\pi\phi)$, and regardless of the choice of $K(\phi) = 0.5 + \cos(0.5\pi\phi)$, convergence remains elusive during Loop 2.

The bridge-load case, as observed in Fig. 18, once again, shows that the inexact method for volume constraint can be problematic during Loop 2. In Loop 2, both $K(\phi) = 1$ and $K(\phi) = 0.5 + \cos(0.5\pi\phi)$ exhibit significant fluctuations in both Fig. 18 and Fig. 19. When considering structural changes during optimization in Fig. 20, the slowest emergence of the structure occurs when using $K(\phi) = 0.5 + \sin(0.5\pi\phi)$, and regardless of the choice of $K(\phi) = 0.5 + \cos(0.5\pi\phi)$, convergence remains elusive during Loop 2. This difficulty in achieving convergence during Loop 2 is inherent to the inexact method for volume constraint, as it operates as an explicit forward time-stepping method and faces challenges when dealing with void domains without mesh.

4. Conclusions

In the context of topology optimization using the exact volume constraint method, we conducted a more extensive investigation considering nonlinear RDE. Our findings indicate that the exact volume constraint remains valid regardless of the choice of $K(\phi)$, and the differences among different $K(\phi)$ options are negligible. The disparity between the FEM mesh used for stress equilibrium and that employed for the reaction-diffusion equation (RDE) of the level set function may be responsible for the convergence issue. As the inexact volume constraint method operates similarly to an explicit time-stepping scheme, instability accumulates within the optimization loop. In this regard, the new exact volume constraint method can stabilize the overall optimization process and is thus more likely to achieve convergence.

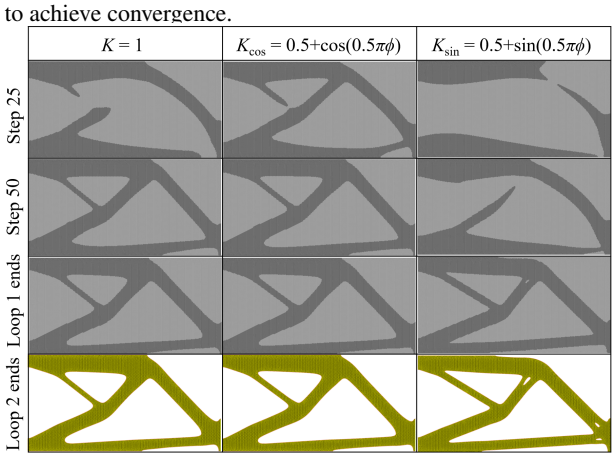

Fig. 8: Structural change by the exact volume constraint method for the lower-load case.

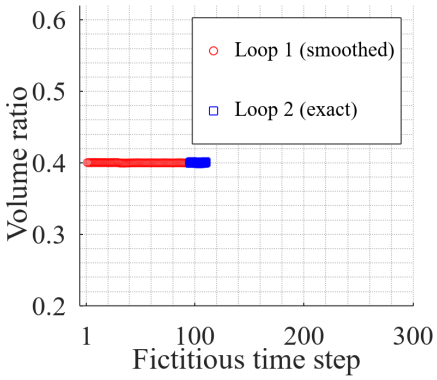

(a) $K(\phi) = 1$

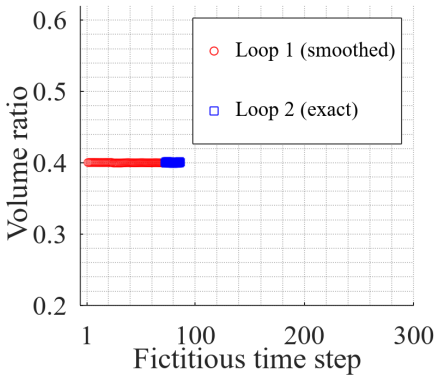

(b) $K(\phi) = 0.5 + \cos(0.5\pi\phi)$

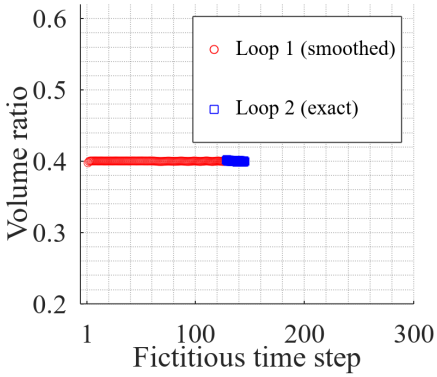

(c) $K(\phi) = 0.5 + \sin(0.5\pi\phi)$

Fig. 9: Volume ratio by the exact volume constraint method for the bridge-like case.

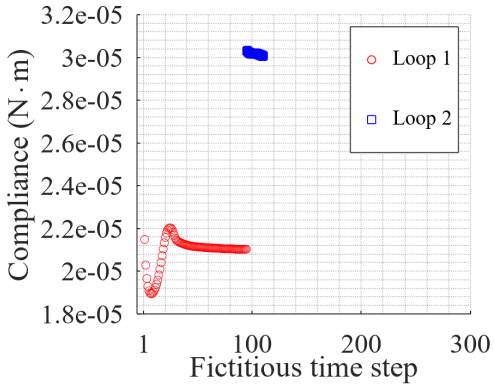

(a) $K(\phi) = 1$

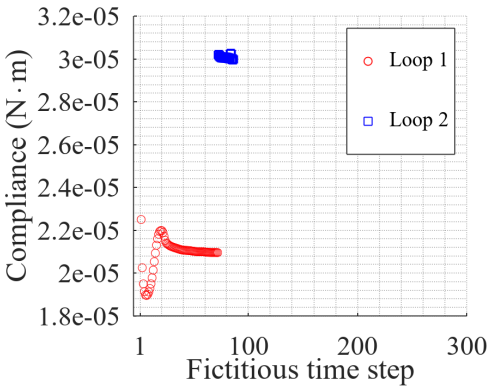

(b) $K(\phi) = 0.5 + \cos(0.5\pi\phi)$

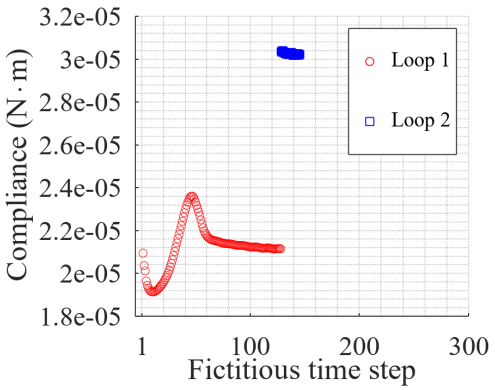

(c) $K(\phi) = 0.5 + \sin(0.5\pi\phi)$

Fig. 10: Structural compliance by using the exact volume constraint method for the bridge-like case considering three different $K(\phi)$.

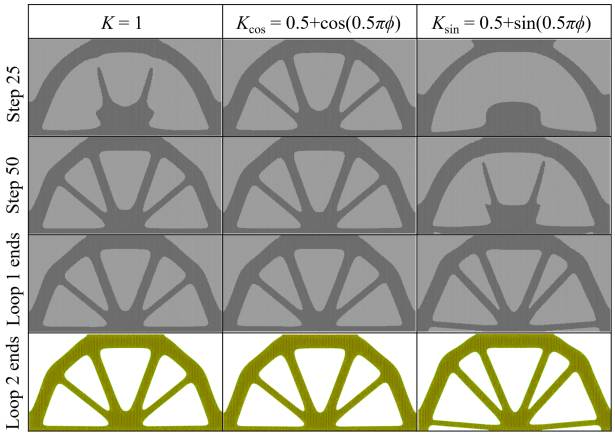

Fig. 11: Structural change during optimization by using the exact volume constraint method for the bridge-like case considering three different $K(\phi)$

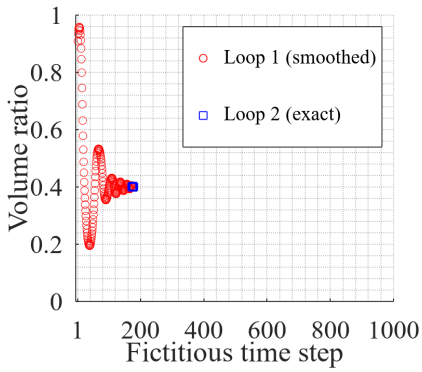

(a) $K(\phi) = 1$

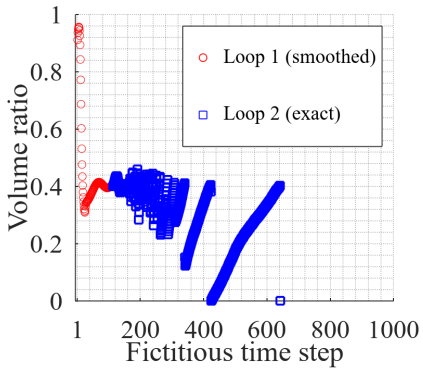

(b) $K(\phi) = 0.5 + \cos(0.5\pi\phi)$

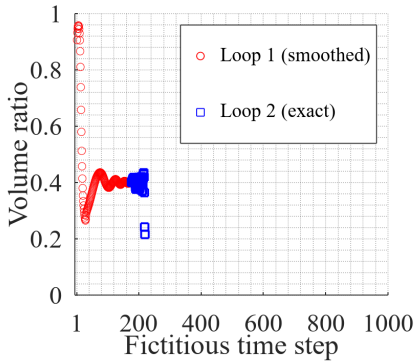

(c) $K(\phi) = 0.5 + \sin(0.5\pi\phi)$

Fig. 12: Volume ratio by using the inexact volume constraint method for the center-load case considering three different $K(\phi)$

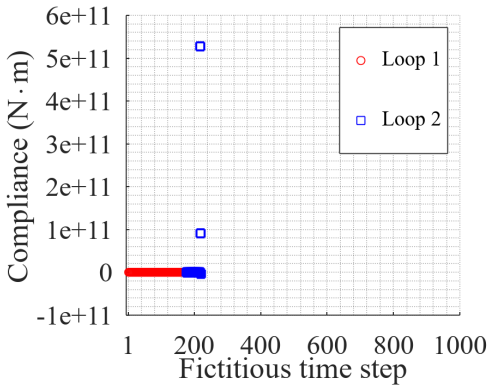

(a) $K(\phi) = 1$

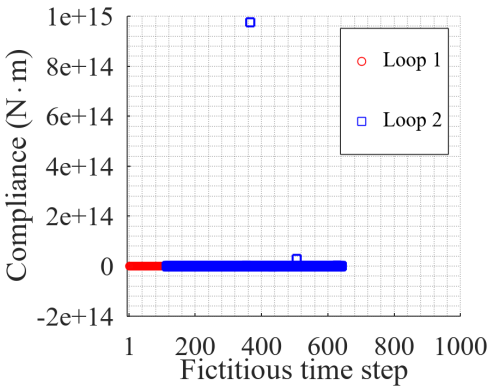

(b) $K(\phi) = 0.5 + \cos(0.5\pi\phi)$

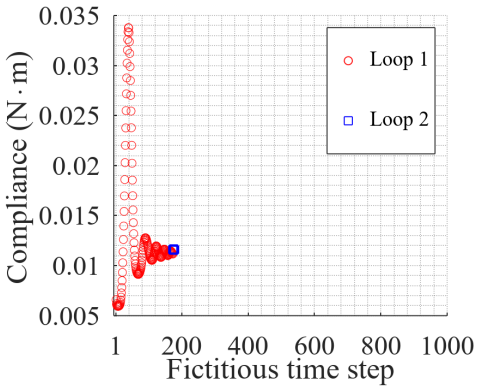

(c) $K(\phi) = 0.5 + \sin(0.5\pi\phi)$

Fig. 13: Structural compliance by using the inexact volume constraint method for the center-load case considering three different $K(\phi)$

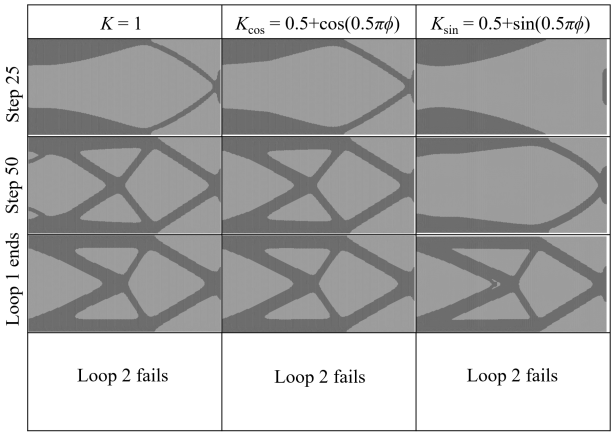

Fig. 14: Structural change during optimization by using the inexact volume constraint method for the center-load case considering three different $K(\phi)$

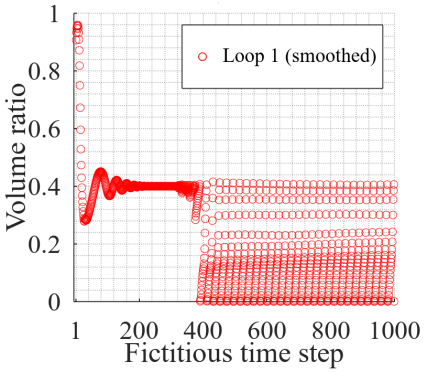

(a) $K(\phi) = 1$

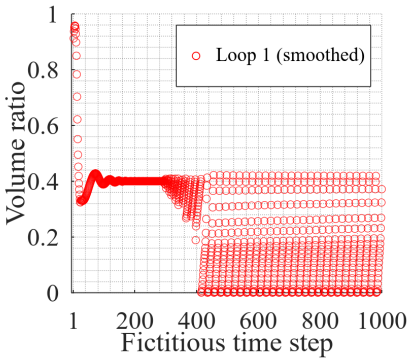

(b) $K(\phi) = 0.5 + \cos(0.5\pi\phi)$

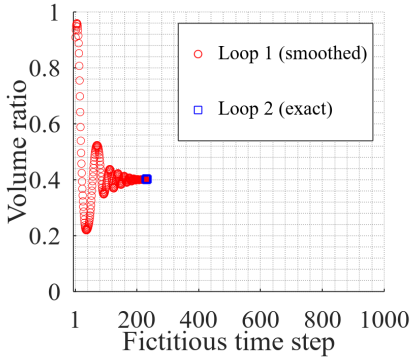

(c) $K(\phi) = 0.5 + \sin(0.5\pi\phi)$

Fig. 15: Volume ratio by using the inexact volume constraint method for the lower-load case considering three different $K(\phi)$

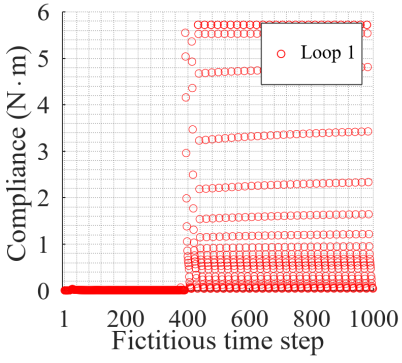

(a) $K(\phi) = 1$

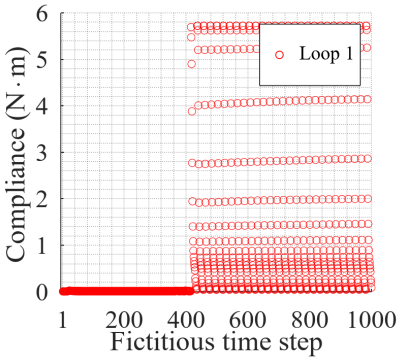

(b) $K(\phi) = 0.5 + \cos(0.5\pi\phi)$

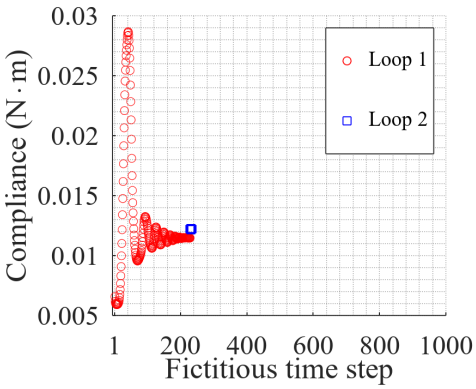

(c) $K(\phi) = 0.5 + \sin(0.5\pi\phi)$

Fig. 16: Structural compliance by using the inexact volume constraint method for the lower-load case considering three different $K(\phi)$

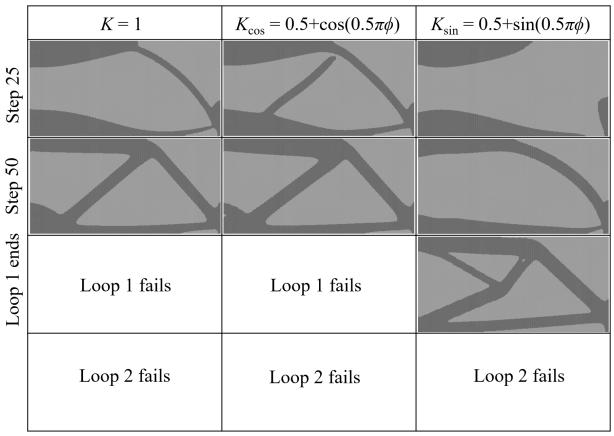

Fig. 17: Structural change during optimization by using the inexact volume constraint method for the lower-load case with different $K(\phi)$

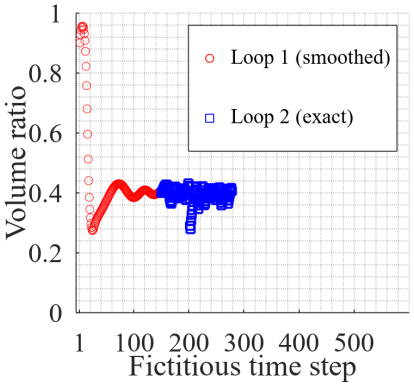

(a) $K(\phi) = 1$

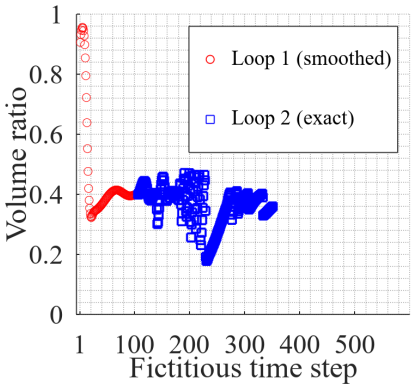

(b) $K(\phi) = 0.5 + \cos(0.5\pi\phi)$

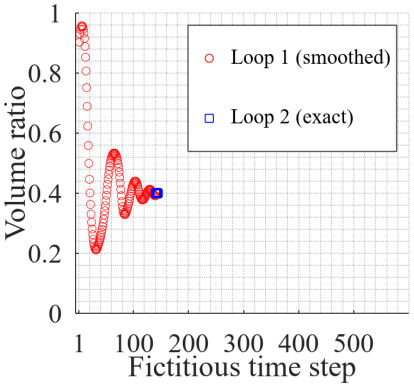

(c) $K(\phi) = 0.5 + \sin(0.5\pi\phi)$

Fig. 18: Volume ratio by using the inexact volume constraint method for the bridge-like case with different $K(\phi)$

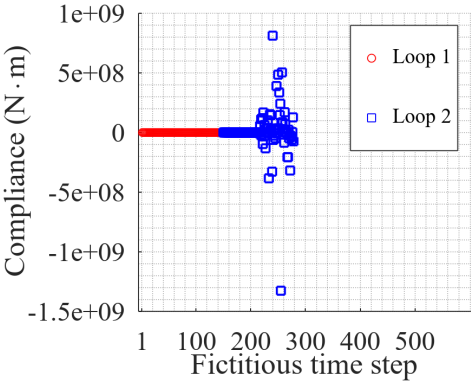

(a) $K(\phi) = 1$

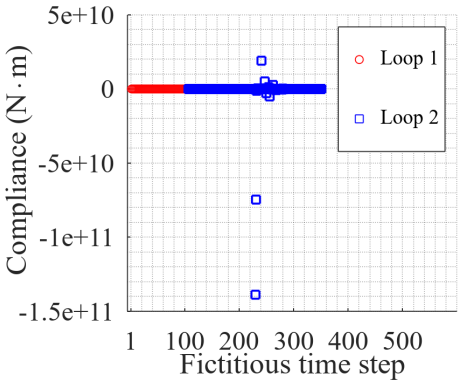

(b) $K(\phi) = 0.5 + \cos(0.5\pi\phi)$

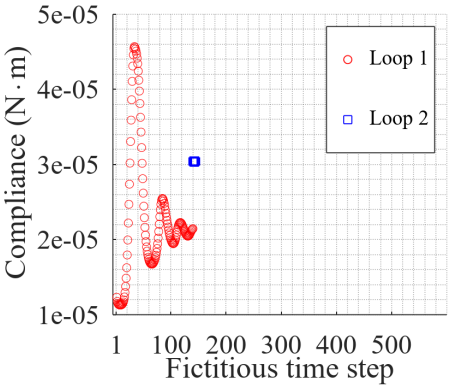

(c) $K(\phi) = 0.5 + \sin(0.5\pi\phi)$

Fig. 19: Structural compliance by using the inexact volume constraint method for the bridge-like case with different $K(\phi)$

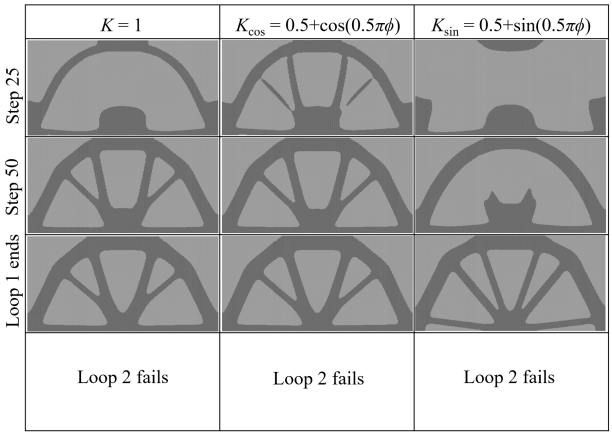

Fig. 20: Structural change during optimization by using the inexact volume constraint method for the bridge-like case with different $K(\phi)$

Reference

(1) Bendsøe, M.P., Sigmund, O.. Material interpolation schemes in topology optimization. Archive of Applied Mechanics (Ingenieur Archiv) Vol.69, No.(9-10), (1999), pp.635-654. doi:10.1007/s004190050248.

(2) Bendsøe, M.P., Sigmund, O.. Topology Optimization. Berlin, Heidelberg: Springer Berlin Heidelberg, (2004), doi:10.1007/978-3-662-05086-6.

(3) Yamada, T., Izui, K., Nishiwaki, S., Takezawa, A.. A topology optimization method based on the level set method incorporating a fictitious interface energy. Computer Methods in Applied Mechanics and Engineering Vol.199, No.45-48, (2010), pp.2876-2891. doi:10.1016/j.cma.2010.05.013.

(4) Emmendoerfer, H., Silva, E.C.N., Fancello, E.A.. Stress-constrained level set topology optimization for design-dependent pressure load problems. Computer Methodsin Applied Mechanics and Engineering Vol.344, (2019), pp.569-601. doi:10.1016/j.cma.2018.10.004.

(5) Zhang, Z., Xie, Y.M., Li, Q., Zhou, S.. A reaction-diffusion based level set method for image segmentation in three dimensions. Engineering Applications of Artificial Intelligence Vol.96, (2020), pp.103998. doi:10.1016/j.engappai.2020.103998.

(6) Li, H., Yamada, T., Jolivet, P., Furuta, K., Kondoh, T., Izui, K., Nishiwaki, S.. Full-scale 3D structural topology optimization using adaptive meshrefinement based on the level-set method. Finite Elements in Analysis and Design Vol.194, (2021), pp.103561. doi:10.1016/j.finel.2021.103561.

(7) Zhuang, Z., Xie, Y., Zhou, S., A reaction diffusion-based level set method using body-fitted mesh for structural topology optimization. Computer Methods in Applied Mechanics and Engineering Vol.381, No.1 (2021), pp. 113829. doi: https://doi.org/10.1016/j.cma.2021.113829.

(8) Zhuang, Z., Xie, Li, Q., Y., Zhou, S., Body-fitted bi-directional evolutionary structural optimization using nonlinear diffusion regularization. Computer Methods in Applied Mechanics and Engineering Vol.396, No.1 (2022), pp. 115114. doi: https://doi.org/10.1016/j.cma.2022.115114.

(9) Cui, Y., and Takahashi, T., and Matsumoto, T., An exact volume constraint method for topology optimization via reaction–diffusion equation. Computers & Structures Vol.280 (2023), pp.1006986.

(10) Cui, Y., and Takahashi, T., and Matsumoto, T., A time-saving FEM-based approach for structural topology optimization with exact boundary representation. Mechanical Engineering Journal, Vol.9, No.6 (2022), pp. 22–00281. https://doi.org/10.1299/mej.22-00281.

(11) Yamada T, Nishiwaki S, Izui K, Yoshimura M, Takezawa A. A Structural Optimization Method Incorporating Level Set Boundary Expressions Based on the Concept of the Phase Field Method. JSMET. 75 (2009) 753 pp. 550–558. https://doi.org/10.1299/kikaia.75.550.

(12) Lopes, C.G., Santos, R.B.d., Novotny, A.A.. Topological derivative based topology optimization of structures subject to multiple loadcases. Latin American Journal of Solids and Structures Vol.12, No.5, (2015), pp.834-860. doi:10.1590/1679-78251252.

(13) Hestenes, M. R.. Multiplier and gradient methods. Journal of Optimization Theory and Applications, Vol. 4, No.5, (1969), pp.303–320. doi:10.1007/BF00927673.

(14) Rockafellar, R. T.. The multiplier method of Hestenes and Powell applied to convex programming. Journal of Optimization Theory and Applications, Vol.12, No.6, (1973), pp.555–562. doi:10.1007/BF00934777.

(15) Powell M. J. D.. Algorithms for nonlinear constraints that use Lagrangian functions. Mathematical Programming, Vol. 14, (1978), pp.224–248. doi:10.1007/BF01588967.

(16) Hecht, F.. New development in freefem++. Journal of Numerical Mathematics Vol.20, No.3-4, (2012), pp. 251-265, doi:10.1515/jnum-2012-0013.

(17) Jolivet, P., Dolean, V., Hecht, F., Nataf, F., Pru' Homme, C., Spillane, N.. High performance domain decomposition methods on massively parallel architectures with freefem++. Journal of Numerical Mathematics vol. 20, no. 3-4, (2012), pp. 287-302. doi:10.1515/jnum-2012-0015.

(18) Kim, C., Jung, M., Yamada, T., Nishiwaki, S., Yoo, J.. FreeFEM++ code for reaction-diffusion equation-based topology optimization: for high-resolution boundary representation using adaptive mesh refinement. Structural and Multidisciplinary Optimization Vol. 62, No.1, (2020), pp.439-455. doi:10.1007/s00158-020-02498-3